NANO LETTERS

pubs.acs.org/NanoLett

Letter

Capillary Balancing: Designing Frost-Resistant Lubricant-Infused Surfaces

William S. Y. Wong,* Katharina I. Hegner, Valentina Donadei, Lukas Hauer, Abhinav Naga, and Doris Vollmer*

Cite This: https://dx.doi.org/10.1021/acs.nanolett.0c02956

Read Online

ACCESS | Metrics & More | Article Recommendations | Supporting Information

ABSTRACT: Slippery lubricant-infused surfaces (SLIPS) have shown great promise for anti-frosting and anti-icing. However, small length scales associated with frost dendrites exert immense capillary suction pressure on the lubricant. This pressure depletes the lubricant film and is detrimental to the functionality of SLIPS. To prevent lubricant depletion, we demonstrate that interstitial spacing in SLIPS needs to be kept below those found in frost dendrites. Densely packed nanoparticles create the optimally sized nanointerstitial features in SLIPS (Nano-SLIPS). The capillary pressure stabilizing the lubricant in Nano-SLIPS balances or exceeds the capillary suction pressure by frost dendrites. We term this concept capillary balancing. Three-dimensional spatial analysis via confocal microscopy reveals that lubricants in optimally structured Nano-SLIPS are not affected throughout condensation (0 °C), extreme frosting (−20 °C to −100 °C), and traverse ice-shearing (−10 °C) tests. These surfaces preserve low ice adhesion (10−30 kPa) over 50 icing cycles, demonstrating a design principle for next-generation anti-icing surfaces.

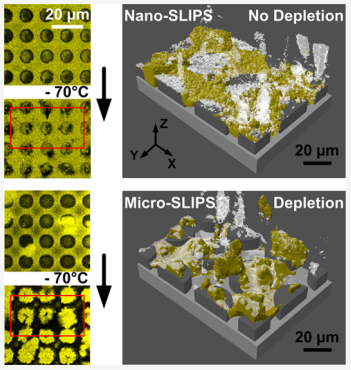

KEYWORDS: *slippery surfaces (SLIPS), anti-icing, anti-frosting, capillary pressure, confocal microscopy*

INTRODUCTION

Frost formation occurs whenever cold surfaces interact with warmer and more humid environments.[1−4] In Nature, frosting is far more prevalent than icing and can be even more detrimental. The formation of frost on wind turbines, power lines, antennas, or heat exchangers affect operational safety, performance, and efficiency.[5,6] Therefore, novel strategies to prevent frost formation are highly desired.[7−10] Among promising anti-icing surfaces,[11−13] slippery liquid-infused porous surfaces (SLIPS) have been discussed for anti-frosting due to frosting-retardant and ultralow ice adhesion properties. The low ice adhesion enables the removal of ice by environmental forces such as vibration or wind shear.[9,14,15] The lubricant layer confers SLIPS with slippery properties, resulting in low liquid, ice, and frost adhesion capabilities. However, the formation of frost at micrometric length scales exerts a strong capillary suction pressure on the lubricant. The lubricant in the porous layer depletes, resulting in direct frost-to-substrate contact.[16−22] When lubricant-covered ice/frost is removed, lubricant which was sucked into frost interstitials is lost.[7,21] Loss of the lubricant leads to increased ice-to-substrate contact and therefore, increased ice adhesion.[7,18]

The pioneering work[14,15,23] of Quéré, Aizenberg, and Varanasi have described the importance of nanostructures in keeping lubricants in place. Aizenberg et al. described the use of nanostructuring in resisting lubricant depletion from body forces.[20] However, these hierarchical surfaces possess micro-interstices, which are susceptible to lubricant depletion. Varanasi et al. studied static equilibrium behaviors of frozen drops with frost, which appear to induce lubricant depletion in both micro- and nanostructured slippery surfaces.[16] Despite the use of nanostructures, lubricant depletion was not prevented, likely due to interstices which are still too large. Therefore, anti-icing and anti-frosting properties of these coatings are potentially ruined after a single frosting event.[16−18] To the best of our knowledge, the understanding and control of frost-induced lubricant depletion is still unresolved. To solve this standing problem and to prevent frost-induced depletion in SLIPS, it is important to correlate the characteristic length scales between the surface and the frost. The capillary suction of oil into frost is governed by surface energy and local curvatures of both entities.

Hoarfrost is one of the most common types of frost found in both man-made and natural environments.[24] In the natural environment, crystal sizes vary between 10 μm[25] and 0.2 m.[26,27] Sizes depend on the intensity of undercooling, air circulation, and the amount of moisture.[28,29] Lubricant depletion induced by micrometric frost may be avoidable by designing smaller interstitial spacing (nanointerstices) in

Received: July 17, 2020
Revised: November 11, 2020

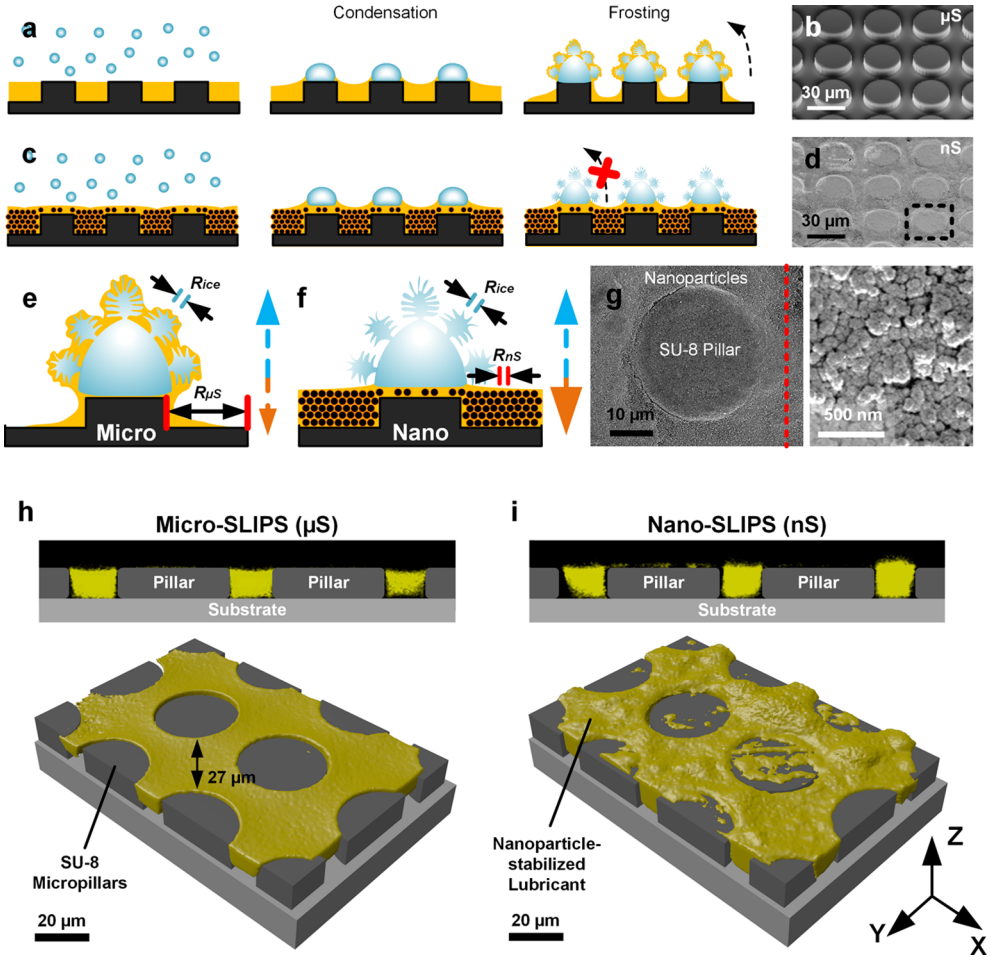

Figure 1. Capillary balancing. SU-8 micropillar arrays are used as invariant visualization markers: They have a height of 10 μm and a diameter of 30 μm. The pitch distance is 40 μm. (a) Sketch of condensation and frost formation on (b) micropillar arrays (Micro-SLIPS, 18 μm, μS, SEM micrograph) resulting in drainage of lubricant from the surface due to strong capillary forces. (c) Sketch of condensation and frost formation on (d) lubricant-infused micropillar arrays filled with nanoparticles (Nano-SLIPS, 30 nm, nS, SEM micrograph). The capillary pressure exerted by nanointerstices keeps lubricants in place. (e) Sketch of capillary balancing: Micro-SLIPS (18 μm) experience strong capillary-induced drainage because of the interstitial spacing R_{ice} imposed by frost-geometries, which falls below those between pillars $R_{ice} < R_{\mu S}$. (f) Capillary-balanced Nano-SLIPS (30 nm, nS) impede capillary-induced drainage by frost R_{ice} due to retentive capillary-forces imposed by nanointerstices R_{nS}. (g) Magnified SEM micrograph of one SU-8 micropillar surrounded by nanoparticles. The nanoparticles and associated interstices are indicated by a representative cross-sectional cut on the right (red dashed line). A high-resolution three-dimensional confocal microscopy image of (h) Micro-SLIPS (18 μm, μS) and (i) Nano-SLIPS (30 nm, nS) under ambient conditions. The yellow color represents the fluorescence from the dyed (Lumogen Red 300, 0.1 mg/mL) lubricant (silicone oil, 200 cSt). The pillars and base substrate are inserted as augmented reality, fitted to experimental confocal surface maps using Blender.

SLIPS (Nano-SLIPS) than that found in frost dendrites. Micron-sized interstices need to be avoided. Therefore, Nano-SLIPS should provide a stabilizing capillary pressure, P_{nS} that exceeds the capillary-induced suction pressure posed by frost dendrites, P_{ice}. We term this design principle "capillary balancing". P_{nS} is approximated by $P_{nS} = \frac{2\gamma}{R_{nS}}$, where γ is the surface tension of the lubricant and R_{ns} is the dimension (characteristic radii) of the nanointerstices. P_{ice} is approximated by $P_{ice} = \frac{2\gamma}{R_{ice}}$, where R_{ice} is the length scale of air gaps between frost dendrites. Can SLIPS follow the design principle of $P_{nS} > P_{ice}$, resulting in long-lasting anti-icing and anti-frosting surfaces?

To test this design principle, we exposed microinterstices-based Micro-SLIPS and nanointerstices-based Nano-SLIPS at low- to ultralow subzero temperatures (−20 °C to −100 °C) to condensation-frosting. To quantify lubricant depletion, we monitored the dynamic condensation-frosting processes using a custom-built confocal microscope. Here, the capillary pressure stabilizing the smallest interstitially spaced Nano-SLIPS (30 nm) dominates over the capillary suction pressure of the frost dendrites, resulting in a stabilized lubricant layer. Under all tested frosting conditions, lubricants in Nano-SLIPS (30 nm) did not suffer from frost-induced capillary depletion. Our design principle successfully achieved frost-resistant anti-icing surfaces, showing a consistently low ice adhesion (N) per unit area (m^2) of between 10 and 30 kPa over 50 icing cycles.

RESULTS AND DISCUSSION

To assess the influence of capillary balancing on condensation-frosting (Figure 1), microstructured SLIPS (Micro-SLIPS, 18 μm, μS, Figure 1a,b, Figure S1) are investigated alongside as-proposed nanostructured SLIPS composed of nanointerstitials (Nano-SLIPS, 30 nm, nS, Figure 1c,d). Micro-SLIPS (18 μm,

https://dx.doi.org/10.1021/acs.nanolett.0c02956
Nano Lett. XXXX, XXX, XXX−XXX

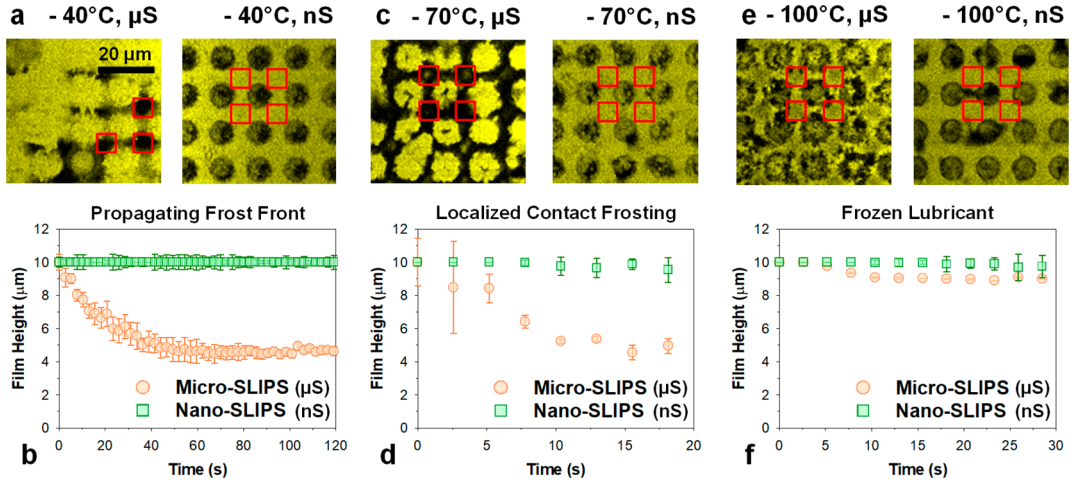

Figure 2. Fluorescence signal (lubricant) of confocal microscopy images of Micro-SLIPS (18 μm, μS) and capillary-balanced Nano-SLIPS (30 nm, nS) under moderate to extreme frosting conditions. (a,c,e) At exposure time, t = 100 s. Top view (XY) images of the frosting behavior, 10× objective. Left panels depict Micro-SLIPS (18 μm, μS) while the right panels depict Nano-SLIPS (30 nm, nS). Different frosting conditions: (a) frost front propagation-induced frosting (−20 °C to −40 °C); (c) localized contact frosting (−50 °C to −70 °C); and (e) thermal reorganization of frozen lubricant (−80 °C to −100 °C). The dark circles show the top faces of the micropillars which are easily observed in Nano-SLIPS (30 nm, nS) even after frost formation. Black grid lines between micropillars are lubricant depleted zones (a,c). (e) Small black irregular regions may depict frost crystals which have grown out of the focal plane. Quantitative dynamic drainage of Micro-SLIPS (18 μm, μS) and Nano-SLIPS (30 nm, nS) at (b) −40 °C, (d) −70 °C, and (f) −100 °C, 100× objective. Location of analysis is always performed on the largest interstitial sites; lubricant heights are averages over the representative area marked in red-colored squares.

μS) have a maximum spacing between pillars (interstices) of $D_{\mu S,max}$ = 27 μm or $D_{\mu S,mean}$ = 18 μm (Figure 1b,h). This corresponds to an effective interstitial radius of $R_{\mu S,mean}$ = 9 μm. The corresponding mean of interstitial spacing ($D_{\mu S/nS,mean}$ or 2 × $R_{\mu S/nS,mean}$) is presented for each variant tested. Nano-SLIPS (30 nm, nS) is comprised of the same micropillar array, infused with a bed of covalently connected (epoxy-amine) nanoparticles (Figure 1d, Supporting Information, Methods).

The range of interstitial spacing in Nano-SLIPS (0−60 nm) shows a mean characteristic length scale, $R_{nS,mean}$, of about 15 nm (Figure 1g, Figure S2), contrasting the interstitial spacing of Micro-SLIPS (10−27 μm), $R_{\mu S,mean}$, at about 9 μm. Differentiating from hierarchical surfaces (micro- and nanostructured), this dense packing of nanoparticles represents a nanostructured layer (between invariant micropillars) that is optimal for capillary balancing. Infusion of the micropillars and the nanoparticle-infused micropillars with silicone oil (Sigma-Aldrich, Silicone oil AR 200, 200 cSt) results in the upper (μS) and lower limits (nS) of Micro-SLIPS (18 μm, μS) and Nano-SLIPS (30 nm, nS) respectively. The silicone oil possesses a glass transitional temperature of about −90 °C, Figure S3. Therefore, we expect significant increase of the viscosity and decrease in fluidity of the silicone oil when approaching the glass transition temperature. The design of Nano-SLIPS (30 nm, nS) is based on our concept of capillary balancing (Figure 1e,f). In contrast to Micro-SLIPS (18 μm, μS, Figure 1e), the smaller length scales in a nanostructured filler provides much stronger capillary retentive forces, thus preventing lubricant depletion during frosting (Figure 1f). R_{ice} was experimentally measured down to about 100−400 nm (Supporting Information, Movie M1), that is, $R_{nS} < R_{ice} < R_{\mu S}$.

We monitored the height and reorganization of lubricant for Micro-SLIPS (18 μm, μS) and Nano-SLIPS (30 nm, nS) using a custom-built laser scanning confocal microscopy (LSCM) setup under a variety of frosting conditions. The 3D reconstructions are obtained from the fluorescence signal of the silicone oil (Supporting Information, Methods).[30] The oil−air interface is noticeably smoother in Micro-SLIPS (18 μm, μS, Figure 1h) as compared to Nano-SLIPS (30 nm, nS, Figure 1i). Here, the micropillars allow for comparative visualization of frosting and depletion dynamics with pillars as location-markers (fixed boundary conditions).

In situ frosting was performed in a custom-built frosting chamber (Supporting Information, Figure S4). The chamber (0.24 L) is inverted, and condensation-frosting is imaged directly from the side facing the objective (about 2−3 mm working distance). The SLIPS variants were mounted on a cooling element with a set-point temperature of between 20 °C to −100 °C. Depending on the set-point temperature, the surface temperature might be a few degrees higher (Supporting Information, Figure S3). If not stated otherwise, all temperatures refer to the set-point temperature. Gas lines deliver dry or wet nitrogen gas into the chamber at 20 °C, 6L/min. To induce frosting, surfaces are cooled down to the set-point temperature under constant dry nitrogen purge and equilibrated for 5 min. Thereafter, a premixed wet nitrogen stream (about 60% RH) is delivered into the chamber for 30 s. The chamber is then sealed as condensation-frosting commences and chamber humidity drops. Confocal microscopy imaging of the surface is performed in parallel, providing *in situ* temporal observations of dynamic processes. This protocol avoids severe frost densification, thus preventing optical scattering of fluorescence. Observation of lubricant reorganization in micropillar arrays is possible despite closer objective-to-frost proximity.

To understand the effect of capillary balancing in dynamic lubricant depletion, we used a low-magnification objective (10×/NA0.40), complemented with a high-magnification objective (100x/NA0.80). The 10× objective allows for high temporal-resolution intensity analysis (Supporting Information, Figure S5). Alternatively, the 100× objective's depth-sensitive numerical aperture allows us to monitor and analyze depletion dynamics in 3D. We mapped the fluorescence and reflection signals with time. As the pillars' tops are facing

https://dx.doi.org/10.1021/acs.nanolett.0c02956
Nano Lett. XXXX, XXX, XXX−XXX

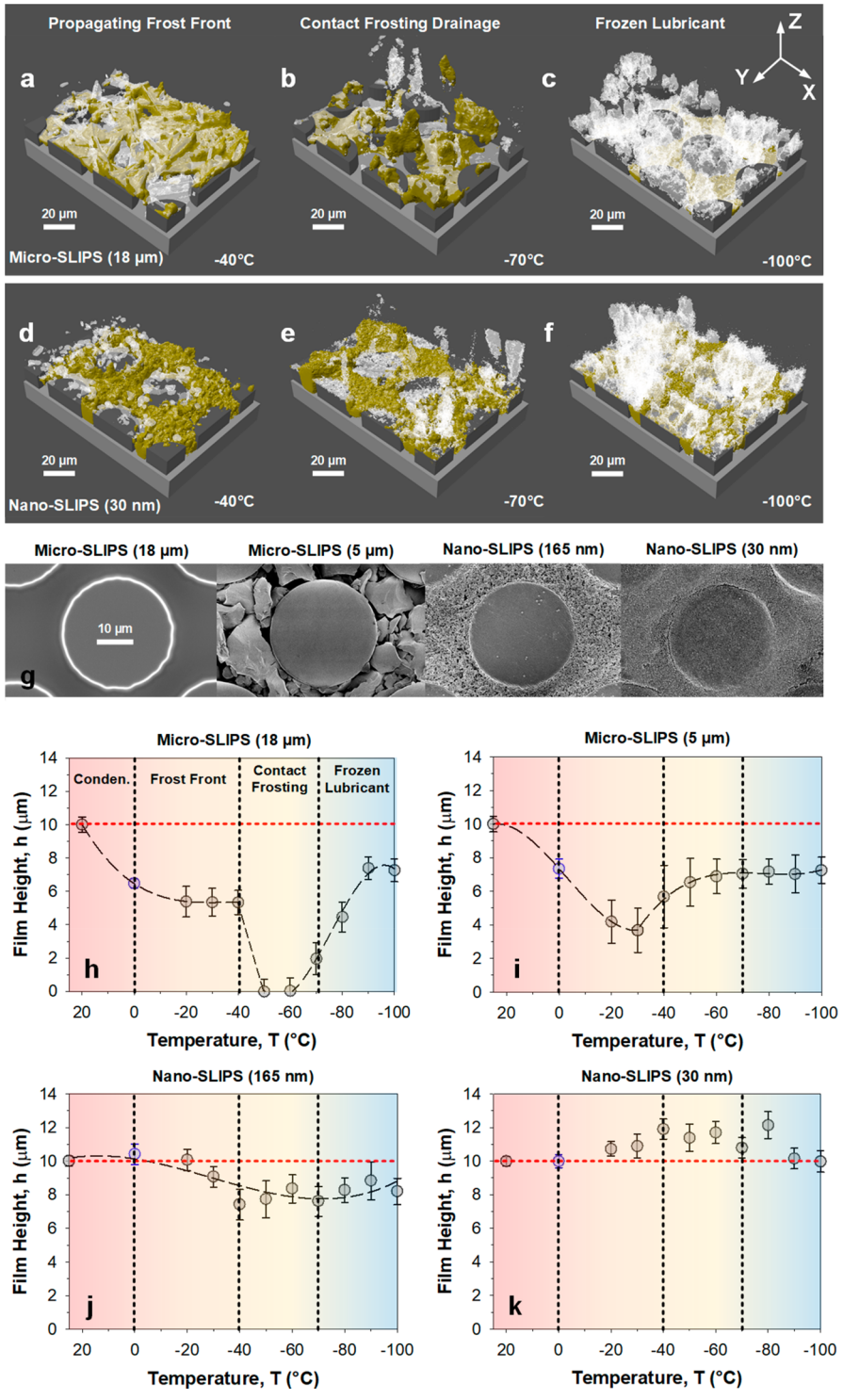

Figure 3. Three-dimensional confocal microscopy imaging for frosting-induced drainage under equilibrium conditions (exposure time, t = 5 min, 100× objective). Micro-SLIPS (18 μm) when exposed to (a) −40 °C, resulting in frost front depletion, (b) −70 °C, contact frosting depletion, and (c) −100 °C, thermal reorganization of molten lubricant. The translucent white surface layer is processed confocal microscopy data, via data from the reflection channel. For Nano-SLIPS (30 nm), the same exposure conditions at (d−f) −40 °C to −100 °C did not appear to induce frosting-induced drainage. (g) In Micro-SLIPS (18 μm), the interstitial spacing varies between 10−27 μm (g, first panel). Depletion occurs almost immediately, even during condensation (second blue data point, h). Depletion increases with lower temperature until they deplete completely between (h) −50 °C to −70 °C. When adding (i) microparticles ($D_{\mu S,mean}$ of 5 μm), the interstitial spacing varies between 0−10 μm. It is zero when particles touch, (g, second panel). (j) For larger nanoparticles ($D_{nS,mean}$ of 165 nm), the interstitial spacing varies between 0−400 nm (g, third panel). For Micro-SLIPS (5 μm) and Nano-SLIPs (165 nm), depletion is noticeably reduced. Lubricant depletion was maximum between −30 °C to −40 °C (about 5 μm) for the former and between −40 °C to −70 °C (about 3 μm) for the latter. Even after the addition of micro- or nanometer-sized particles, interstitial spacing remains too large to prevent lubricant drainage by frost dendrites. The dashed lines serve to guide the eye. (k) For Nano-SLIPS (30 nm) with an interstitial spacing of between 0−60 nm (g, fourth panel), they appear to resist depletion with an undepleted base height throughout experiments. The lubricant, silicone oil (yellow) was dyed with Lumogen Red 300 at 0.1 mg/mL.

https://dx.doi.org/10.1021/acs.nanolett.0c02956
Nano Lett. XXXX, XXX, XXX−XXX

toward the objective, depletion can be monitored at a vertical resolution of about 1 μm and a horizontal resolution of 0.2 μm. Macroscopic top-down static images (10× objective) of lubricant (yellow) on Micro-SLIPS (18 μm, μS) are presented on the left and Nano-SLIPS (30 nm, nS) on the right (Figure 2). The analysis is typically performed within interstitial sites (Figure 2a,c,e, red squares, Figure S6) between pillars to provide additional micromacroscopic intuition behind frosting-induced lubricant reorganization. We observe the following three dominant modes of frosting and lubricant reorganization: (1) propagating frost front (−20 °C to −40 °C), (2) localized contact frosting with the formation of frost crowns (−50 °C to −70 °C), and (3) thermal reorganization of frozen lubricants due to latent-heat effects (−80 °C to −100 °C). For conciseness, we discuss the −40 °C, −70 °C, and −100 °C states as representative of these respective modes (Figure S5 and S7 for different temperatures).

At −20 °C to −40 °C, we observe that frosting is triggered by nucleation at a random spot. Frost spreads outward from these spots in a quasi-circular front that sweeps over the entire observable domain (Movie M2). On Micro-SLIPS (18 μm, μS), the frost front moved at a velocity of about 8 ± 1 μm/s, forming frost dendrites that suck lubricant (yellow) up into the frost structures as they form (Figure 2a, μS). This partially empties the large lubricant-filled interstices surrounding the frost (Figure 2b, Figures S5−7). After frost growth and propagation stops, no further lubricant is absorbed and the film height stabilizes. Note that as soon as the chamber's relative humidity drops below about 5−10% (temperature-sensitive), frosting stops (Supporting Information, Table 1). Measurement errors result from frost propagation-induced spatial shifts (inhomogeneities) in frosting and lubricant depletion. In contrast to Micro-SLIPS (18 μm, μS), the lubricant height in the capillary-balanced Nano-SLIPS (30 nm, nS) stayed at about 10 μm throughout the frosting process (despite frost growth, Movie M2). This demonstrates an innate stability of the nanoparticle-stabilized lubricant layer (Figure 2a,b, Figures S5 and S7).

At the set-points of −50 °C to −70 °C, the substrate surface is well below −39 °C (Figure 2c,d, Figure S3). This is the critical temperature at which contacting water vapor freezes immediately, regardless of surface-based nucleation sites.[31] On Micro-SLIPS (18 μm, μS) at −70 °C, frost forms around each pillar, giving rise to crownlike domains surrounding each pillar (Figure 2c, μS and Movie M3). This results in a rapid drainage of lubricant in its local vicinity (Figure 2d, circles). The completion of drainage occurred in just about 10 s of exposure, alongside a decrease of lubricant height by about 6 μm. As contact frosting is highly localized, the time scale of depletion in this temperature range is significantly faster compared to depletion at higher temperatures. The experiment was not evaluated beyond 20 s due to frost densification that reduces optical contrast for high temporal scan resolutions. Once again, capillary-balanced Nano-SLIPS (30 nm, nS) demonstrate a lubricant layer that is largely stable within the same time (Figure 2d, squares) and temperature domain (Figures S5 and S7).

At even colder temperatures, we reach the domain where the lubricant begins to freeze/solidify (set-point of −80 °C to −100 °C). The lubricant is completely frozen at set-points of −90 °C to −100 °C (Figure 2e, Figures S7 and Movie M4). With Micro-SLIPS (18 μm, μS) at −100 °C, the lubricant height still decreased by about 2 μm during frosting after a small time-delay (10 s) although the lubricant should be frozen (Figure 2f, circles). This might be caused by the localized melting and reorganization of solidified lubricant, as latent heat is released from the condensation and frosting of water. As before, the measurement was terminated after 30 s of exposure due to frost densification, as the underlying lubricant-infused micropillar array becomes obscured. The capillary-balanced lubricant layer in Nano-SLIPS (30 nm, nS) remained stable within the same time domain (Figure 2f, squares).

As frost densification obscures the direct observation of lubricants and height measurement after 20−30 s of exposure under ultracold temperatures (−50 °C to −100 °C), detailed information at equilibrium remains unknown. Nonetheless, the final state of frosting and lubricant depletion can still be obtained by performing high-resolution 3D scans (50 μm height, 0.25 μm resolution, 32-line scans, Figure 3). The 3D reconstructions of the overlaid reflection (translucent white) and fluorescence (yellow) channels are then coupled to an augmented array of micropillars (gray) for visualization (Figure S8). Note: The reflection signal represents a frosted ice layer if no fluorescence signals are overlapping. It is also important to acknowledge that fine frost structures may cause scattering.

Frost on Micro-SLIPS (18 μm). At −40 °C, frost dendrites (about 2−3 μm layer) have a rodlike shape and a diameter of 1.9 ± 0.5 μm (Figure 3a, Figure S9). Notably, even the uppermost parts of the frost dendrites are covered in lubricants. At −70 °C, frost appeared to be agglomerate-like with submicron features. The submicron frost features efficiently soaked lubricants up to about 20−30 μm above pillar tops, deep into the frost layer (Figure 3b and Figure S9). At −100 °C, these submicron features persisted (Figure 3c and Figure S9). The frost is porous and dendritic, Movie M1.

Fluorescence signals within the micrometric interstitial spacing ($D_{\mu S,\mathrm{mean}}$) = 18 μm, Figure 3g, first panel) are analyzed as equilibrium heights. Lubricant depletion occurs immediately upon condensation (Figure 3h, blue symbol at 0 °C). This is attributed to the formation of wetting ridges around condensed droplets.[32] Between −20 °C to −40 °C, the propagation of a frost front results in partial depletion of lubricant within the interstices (Figure 3h, Figure 1h, orange domain). Some lubricant is left in the interstices between the micropillars (gray areas). Depending on the exact location chosen for analysis, the degree of depletion may differ. The improved height and intensity resolution of these so-termed equilibrium scans reveal that lubricant heights in the interstices decrease to near-zero at temperatures between −40 °C to −70 °C (Figure 3h, yellow domain). At even colder temperatures of between −70 °C to −100 °C, the degree of depletion decreases, due to a semifrozen lubricant layer. However, a slightly depleted height of about 8 μm ± 1 μm is still detectable (Figure 3c,h). This decrease in lubricant height within pillars' interstices hints of a latent heat effect during frosting, which induces localized melting and reorganization of the frozen lubricant (Supporting Information).

Scaling Micro-SLIPS to Nano-SLIPS. To provide a description of scale, variations of both Micro-SLIPS and Nano-SLIPS were designed using different filler microparticles (Figure 3g, second panel) and nanoparticles (Figure 3g, third panel), respectively. The resulting range of interstitial spacings are between 0−10 μm and 0−400 nm, respectively. Interstitial spacings were determined by thresholding and 500 sampling circle fits using ImageJ. It appears that the supplementary use of micro- to nanoscale particles promotes lubricant retention

https://dx.doi.org/10.1021/acs.nanolett.0c02956
Nano Lett. XXXX, XXX, XXX−XXX

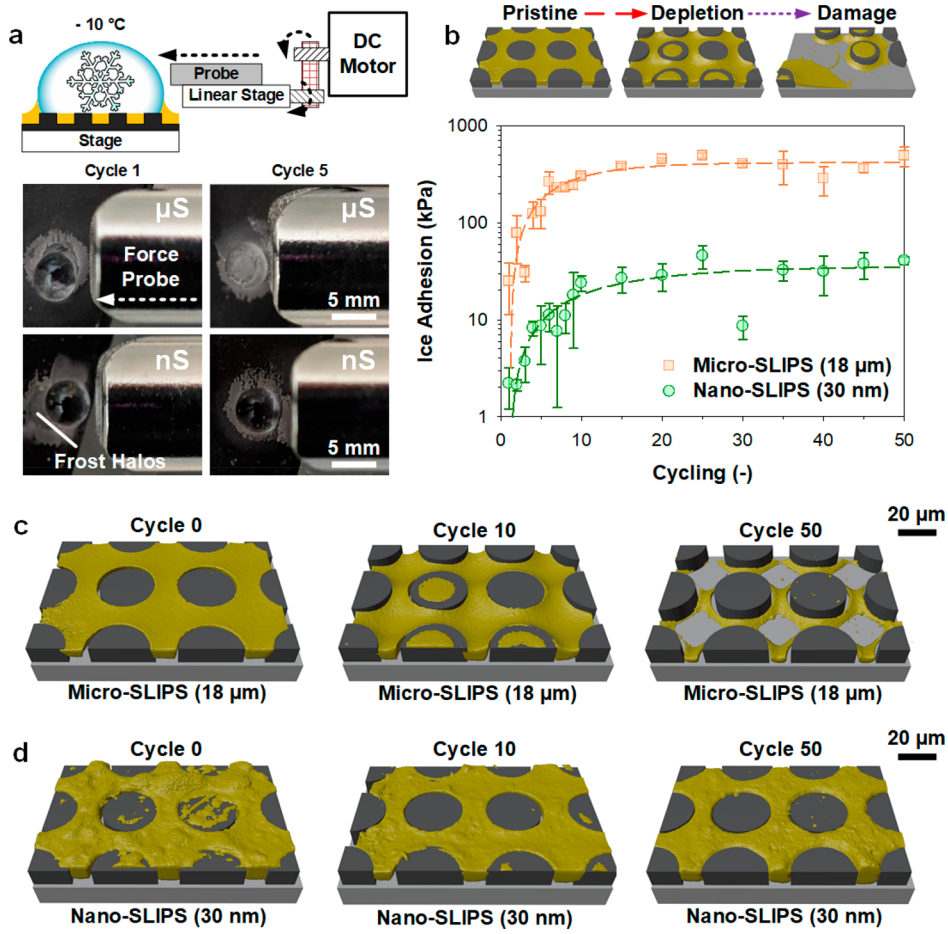

Figure 4. Influence of freezing and associated drainage dynamics on anti-icing adhesion performance. (a) A custom-built setup was designed for ice adhesion measurements at −10 °C. Water drops of 10 μL (diameter of about 0.6 cm) were deposited on surfaces: Micro-SLIPS (18 μm, μS, top panels) and Nano-SLIPS (30 nm, nS, bottom panels) and frozen. Thereafter, a force probe (sensitivity of 0.01 N, contact point: 0.5 mm above the surface) is driven toward the ice drop at about 30 μm/s until the ice drops are detached. The continuous force curves were collected and the peak-forces measured. (b) The capillary-balanced Nano-SLIPS (30 nm, nS) variants kept their excellent low surface adhesion (N) per unit area (m^2) to ice drops during cyclic testing (<20 kPa) up to 10th cycle and equilibrated at about 30 kPa by the 50th cycle. (c,d) Notably, near-complete lubricant depletion occurred for (c) Micro-SLIPS (18 μm, μS) as compared to a nearly unaffected lubricant layer for (d) Nano-SLIPS (30 nm, nS). By the 10−50th cycles, Nano-SLIPS (30 nm, nS) appear to be significantly more uniform as compared to the pristine version. This is attributed to the direct removal of inhomogeneous asperities during ice shear and removal.

with smaller interstices (Figure 3h,i). However, the maximum extent of drainage in these variants: Micro-SLIPS (5 μm) and Nano-SLIPS (165 nm), remains significant (about 3−6 μm). Nonetheless, drainage is still notably reduced compared to Micro-SLIPS (18 μm). Lubricant drainage reaches about 6 μm between −20 °C to −40 °C for Micro-SLIPS (5 μm) and about 3 μm between −40 °C to −70 °C for Nano-SLIPS (165 nm). With a further decrease in temperatures we noted reduced extents of depletion, likely because of increasing lubricant viscosity when approaching the glass transition temperature (−90 °C). Lubricant heights reach a final steady value of about 7−9 μm at −100 °C. This improved lubricant retention behavior is likely caused by the partial success (Figure 3i,j, Figure S10) of capillary balancing, relevant at nanometer length scales.

Frost on Nano-SLIPS (30 nm). First, frost morphology differs slightly at warmer temperatures (compared to aforementioned SLIPS variants). At −40 °C, the frost appears to be significantly more spherical or cuboidal in shape, at diameters of 4.1 ± 0.9 μm (Figure 3d and Figure S9). Below −40 °C, frost appears agglomerate-like with submicron features, which persists even at −100 °C within a similar length scale (Figure 3e,f and Figure S9). Frost was also detected up to a height of 30 μm above pillar tops. At all exposure temperatures, pillar tops remain free of lubricant and the interstices between pillars remain filled with lubricant. These results showcase the core discovery: Dense nano-structuring is required for capillary balancing (interstitial spacing of 0−60 nm). Hierarchical surfaces should not work due to the presence of large microinterstices where lubricant can be drained. High capillary retention requires surfaces that possess only densely spaced geometries with nanointerstices.

On Nano-SLIPS (30 nm), we did not observe lubricant drainage after the condensation of water droplets (Figure 3h, blue data point). Notably, throughout the entire temperature range (−20 °C to −100 °C), no lubricant depletion within the bulk phase was observed within experimental resolution. At a few locations, some lubricant was observed at 1−2 μm above its initial height. This small increase was predominantly found from −40 °C to −80 °C (Figure 3h). Lower temperatures have been observed to lead to finer frost crystals and potentially higher capillary suction. Therefore, tiny amounts of excess

https://dx.doi.org/10.1021/acs.nanolett.0c02956
Nano Lett. XXXX, XXX, XXX−XXX

lubricant (after infusion) that are not nanointerstitially retained may be easily drawn into the frost. This excess lubricant was not removed postsynthesis (i.e., by washing) as the Micro-SLIPS and Nano-SLIPS configurations were treated identically to ensure a fair comparison. While minor traces of excess lubricant are likely a primary cause for our observations, the possibility of cloaking is also discussed (Supporting Information, Lubricant-Cloaked Frost Ice).

Influence of Frosting on Ice Adhesion Behavior. We now question what consequences frosting and capillary-balancing have on icing and deicing in SLIPS (Figure 4). Essentially, icing rarely occurs independently from frosting. To quantify ice adhesion strength, Micro-SLIPS (18 μm, μS) and Nano-SLIPS (30 nm, nS) were enclosed in an icing chamber kept at −10 °C. Upon equilibrium, a small drop of water (10 μL) is deposited on its surface and allowed to freeze (Figure 4a). Frost halos[33] are formed from the drops' surrounding vapor gradients during delayed freezing. Upon solidification, a force sensor is automatically driven toward the frozen ice drop at 30 μm/s until ice detachment (Figure 4a). The recorded force reaches a maximum peak, thereafter dropping to 0 N (Figure S11). This corresponds to the moment when the ice drop detaches from the surfaces. Fifty deicing cycles were performed over three locations. The maximum forces (N) recorded are divided by the contact area (m^2) of frozen drops and averaged. Thus, ice adhesion strength is computed in Pa (Figure 4b).

Micro-SLIPS (18 μm, μS, Figure 4b, orange squares) experience a gradual rise in ice adhesion. This rise originates from a gradual depletion of lubricant volume, as confirmed by confocal microscopy (Figure 4b, depletion inset). Occasional large errors in force measurements were caused by contact-shear damage of the pillars, leading to a lubricant depleted zone with direct ice contact and very high ice adhesion (Figure 4b, damage inset). After 50 cycles, ice adhesion strength leveled off. Micro-SLIPS (18 μm, μS) were almost completely drained of lubricant by the 50th cycle (Figure 4c). In contrast, Nano-SLIPS (30 nm, nS) experience a consistently low ice adhesion (<30 kPa) even after 50 deicing cycles (Figure 4b, green circles) with no noticeable loss of lubricant (Figure 4d). However, adhesion did increase from about 2−18 kPa by the 10th cycle. This may be caused by removal of tiny amounts of excess lubricant and excess nanoparticle agglomerates (i.e., tops of pillars) originating from sample preparation. By the 10th cycle, the originally rough pristine nanoparticle-infused lubricant domains are now notably smoother (Figure 4d). In contrast to Micro-SLIPS (18 μm, μS), the integration of densely packed nanoparticles within the micropillar arrays may have also enhanced the overall mechanical stability. Therefore, the lubricant layer in Nano-SLIPS (30 nm, nS) remains stable and functional (30 ± 10 kPa) even after 50 cycles (Figure 4d).

CONCLUSIONS

The severe problem of lubricant depletion in SLIPS during frosting and icing can be prevented if the interstitial spacing of the infused surface is smaller than that between frost dendrites. To avoid capillary-suction induced depletion, the design principle of "capillary balancing" needs to be followed: All nanointerstitial spacing needs to be lesser than those found in frost dendrites. If not, lubricant depletion can be reduced but not avoided. Dense packing of small nanoparticles (in the order of 10 nm) creates effective nanoscale interstitial spacing. Densified nanostructured packing is shown to preserve performance even after multiple traverse shear icing−deicing cycles. After 10 cycles, ice adhesion per unit area remains as low as 12 ± 4 kPa and levels off at 30 kPa after 50 cycles. In contrast, the microstructured variation reaches an ice adhesion of 500 kPa after 50 cycles. The design principle of capillary balancing allows for the development of frost-resistant, durable anti-icing lubricant-infused surfaces that may survive extreme terrestrial (−20 °C to −70 °C) and even extra-terrestrial environments (<−70 °C).

ASSOCIATED CONTENT

Supporting Information

The Supporting Information is available free of charge at https://pubs.acs.org/doi/10.1021/acs.nanolett.0c02956.

Methods (synthesis and characterization), supplementary discussion (cloaking), and supplementary figures (supplementary characterization) (PDF)

M1: 3D reconstruction of frost agglomerates; 360° rotation (AVI)

M2: Micro-SLIPS versus Nano-SLIPS during frosting at −40 °C; real-time, 1× speed (AVI)

M3: Micro-SLIPS versus Nano-SLIPS during frosting at −70 °C; real-time, 1× speed (AVI)

M4: Micro-SLIPS versus Nano-SLIPS during frosting at −100 °C; real-time, 1× speed (AVI)

M5: Lubricant-mobility in Micro-SLIPS during cooling from −40 °C to −100 °C; 10× speed (AVI)

AUTHOR INFORMATION

Corresponding Authors

William S. Y. Wong − *Max Planck Institute for Polymer Research, D-55128 Mainz, Germany;* orcid.org/0000-0002-5389-5018; Email: wong@mpip-mainz.mpg.de

Doris Vollmer − *Max Planck Institute for Polymer Research, D-55128 Mainz, Germany;* orcid.org/0000-0001-9599-5589; Email: vollmerd@mpip-mainz.mpg.de

Authors

Katharina I. Hegner − *Max Planck Institute for Polymer Research, D-55128 Mainz, Germany*

Valentina Donadei − *Max Planck Institute for Polymer Research, D-55128 Mainz, Germany; Faculty of Engineering and Natural Sciences, Tampere University, FI-33014 Tampere, Finland;* orcid.org/0000-0001-9382-8613

Lukas Hauer − *Max Planck Institute for Polymer Research, D-55128 Mainz, Germany*

Abhinav Naga − *Max Planck Institute for Polymer Research, D-55128 Mainz, Germany*

Complete contact information is available at: https://pubs.acs.org/10.1021/acs.nanolett.0c02956

Author Contributions

W.S.Y.W. and K.I.H. fabricated the surfaces. W.S.Y.W. carried out the experiments and characterization unless otherwise stated below and wrote the manuscript. W.S.Y.W and K.I.H. performed scanning electron microscopy and discussed (with L.H.), confocal microscopy results. V.D. aided in supplementary confirmation experiments. W.S.Y.W. performed the image processing with L.H.'s consultation. All authors (particularly W.S.Y.W, L.H., A.N., and D.V.) discussed the mechanisms for understanding capillary balancing. W.S.Y.W. and D.V. contributed to experimental planning, data analysis,

https://dx.doi.org/10.1021/acs.nanolett.0c02956
Nano Lett. XXXX, XXX, XXX−XXX

and manuscript preparation. All authors reviewed and approved the manuscript.

Notes

The authors declare no competing financial interest.

■ ACKNOWLEDGMENTS

This work was supported by the European Union's Horizon 2020 research and innovation program LubISS No. 722497 (W.W., A.N., V.D., D.V.), the German Research Foundation (DFG) with the Priority Programme 2171 (L.H., D.V.), the Collaborative Research Center 1194 (L.H.), the Max Planck − Univ. Twente Center for Complex Fluid Dynamics (D.V.), and the Max Planck Graduate Center (K.I.H.). We thank M. D'Acunzi, H.-J. Butt, and P. Baumli for stimulating discussions and A. Sharifi for technical support.

■ REFERENCES

(1) Oliver, J. E. *Encyclopedia of World Climatology*; Springer Netherlands: Dordrecht, The Netherlands, 2008.
(2) Na, B.; Webb, R. L. A Fundamental Understanding of Factors Affecting Frost Nucleation. *Int. J. Heat Mass Transfer* **2003**, *46*, 3797−3808.
(3) Sastry, S. Ins and Outs of Ice Nucleation. *Nature* **2005**, *438*, 746−747.
(4) Guadarrama-Cetina, J.; Mongruel, A.; González-Viñas, W.; Beysens, D. Percolation-Induced Frost Formation. *EPL* **2013**, *101*, 16009.
(5) Nath, S.; Ahmadi, S. F.; Boreyko, J. B. A Review of Condensation Frosting. *Nanoscale Microscale Thermophys. Eng.* **2017**, *21*, 81−101.
(6) Petit, J.; Bonaccurso, E. General Frost Growth Mechanism on Solid Substrates with Different Stiffness. *Langmuir* **2014**, *30*, 1160−1168.
(7) Kreder, M. J.; Alvarenga, J.; Kim, P.; Aizenberg, J. Design of Anti-Icing Surfaces: Smooth, Textured or Slippery? *Nat. Rev. Mater.* **2016**, *1*, 15003.
(8) Niemelä-Anttonen, H.; Koivuluoto, H.; Tuominen, M.; Teisala, H.; Juuti, P.; Haapanen, J.; Harra, J.; Stenroos, C.; Lahti, J.; Kuusipalo, J.; Mäkelä, J. M.; Vuoristo, P. Icephobicity of Slippery Liquid Infused Porous Surfaces under Multiple Freeze-Thaw and Ice Accretion-Detachment Cycles. *Adv. Mater. Interfaces* **2018**, *5*, 1800828.
(9) Kim, P.; Wong, T.-S.; Alvarenga, J.; Kreder, M. J.; Adorno-Martinez, W. E.; Aizenberg, J. Liquid-Infused Nanostructured Surfaces with Extreme Anti-Ice and Anti-Frost Performance. *ACS Nano* **2012**, *6*, 6569−6577.
(10) Lv, J.; Song, Y.; Jiang, L.; Wang, J. Bio-Inspired Strategies for Anti-Icing. *ACS Nano* **2014**, *8*, 3152−3169.
(11) Meuler, A. J.; Smith, J. D.; Varanasi, K. K.; Mabry, J. M.; McKinley, G. H.; Cohen, R. E. Relationships between Water Wettability and Ice Adhesion. *ACS Appl. Mater. Interfaces* **2010**, *2*, 3100−3110.
(12) Golovin, K.; Kobaku, S. P. R.; Lee, D. H.; DiLoreto, E. T.; Mabry, J. M.; Tuteja, A. Designing Durable Icephobic Surfaces. *Sci. Adv.* **2016**, *2* (3), No. e1501496.
(13) Schwarzer, M.; Otto, T.; Schremb, M.; Marschelke, C.; Tee, H. T.; Wurm, F. R.; Roisman, I. V.; Tropea, C.; Synytska, A. Supercooled Water Drops Do Not Freeze During Impact on Hybrid Janus Particle-Based Surfaces. *Chem. Mater.* **2019**, *31*, 112−123.
(14) Lafuma, A.; Quéré, D. Slippery Pre-Suffused Surfaces. *EPL* **2011**, *96*, 56001.
(15) Wong, T. S.; Kang, S. H.; Tang, S. K.; Smythe, E. J.; Hatton, B. D.; Grinthal, A.; Aizenberg, J. Bioinspired Self-Repairing Slippery Surfaces with Pressure-Stable Omniphobicity. *Nature* **2011**, *477*, 443−7.
(16) Rykaczewski, K.; Anand, S.; Subramanyam, S. B.; Varanasi, K. K. Mechanism of Frost Formation on Lubricant-Impregnated Surfaces. *Langmuir* **2013**, *29*, 5230−5238.
(17) Subramanyam, S. B.; Rykaczewski, K.; Varanasi, K. K. Ice Adhesion on Lubricant-Impregnated Textured Surfaces. *Langmuir* **2013**, *29*, 13414−13418.
(18) Irajizad, P.; Nazifi, S.; Ghasemi, H. Icephobic Surfaces: Definition and Figures of Merit. *Adv. Colloid Interface Sci.* **2019**, *269*, 203−218.
(19) Peppou-Chapman, S.; Neto, C. Mapping Depletion of Lubricant Films on Antibiofouling Wrinkled Slippery Surfaces. *ACS Appl. Mater. Interfaces* **2018**, *10*, 33669−33677.
(20) Kim, P.; Kreder, M. J.; Alvarenga, J.; Aizenberg, J. Hierarchical or Not? Effect of the Length Scale and Hierarchy of the Surface Roughness on Omniphobicity of Lubricant-Infused Substrates. *Nano Lett.* **2013**, *13*, 1793−1799.
(21) Baumli, P.; Teisala, H.; Bauer, H.; Garcia-Gonzalez, D.; Damle, V.; Geyer, F.; D'Acunzi, M.; Kaltbeitzel, A.; Butt, H.-J.; Vollmer, D. Flow-Induced Long-Term Stable Slippery Surfaces. *Adv. Sci.* **2019**, *6*, 1900019.
(22) Kreder, M. J.; Daniel, D.; Tetreault, A.; Cao, Z.; Lemaire, B.; Timonen, J. V. I.; Aizenberg, J. Film Dynamics and Lubricant Depletion by Droplets Moving on Lubricated Surfaces. *Phys. Rev. X* **2018**, *8*, 031053.
(23) Smith, J. D.; Dhiman, R.; Anand, S.; Reza-Garduno, E.; Cohen, R. E.; McKinley, G. H.; Varanasi, K. K. Droplet Mobility on Lubricant-Impregnated Surfaces. *Soft Matter* **2013**, *9*, 1772−1780.
(24) Laforte, J. L.; Allaire, M. A.; Laflamme, J. State-of-the-Art on Power Line De-Icing. *Atmos. Res.* **1998**, *46*, 143−158.
(25) Kameda, T.; Yoshimi, H.; Azuma, N.; Motoyama, H. Observation of "Yukimarimo" on the Snow Surface of the Inland Plateau, Antarctic Ice Sheet. *J. Glaciol.* **1999**, *45*, 394−396.
(26) Perşoiu, A. Ice Caves Climate. In *Ice Caves*; Perşoiu, A., Lauritzen, S.-E., Eds.; Elsevier, 2018; Chapter 3, pp 21−32.
(27) Knight, C. A.; Devries, A. L. Growth Forms of Large Frost Crystals in the Antarctic. *J. Glaciol.* **1985**, *31*, 127−135.
(28) Léoni, A.; Mondot, M.; Durier, F.; Revellin, R.; Haberschill, P. State-of-the-Art Review of Frost Deposition on Flat Surfaces. *Int. J. Refrig.* **2016**, *68*, 198−217.
(29) Le Gall, R.; Grillot, J. M.; Jallut, C. Modelling of Frost Growth and Densification. *Int. J. Heat Mass Transfer* **1997**, *40*, 3177−3187.
(30) Butt, H. J.; Kappl, M. *Surface and Interfacial Forces*, 2nd ed.; Wiley-VCH: Weinheim, Germany, 2018.
(31) Koop, T.; Luo, B.; Tsias, A.; Peter, T. Water Activity as the Determinant for Homogeneous Ice Nucleation in Aqueous Solutions. *Nature* **2000**, *406*, 611−614.
(32) Kajiya, T.; Schellenberger, F.; Papadopoulos, P.; Vollmer, D.; Butt, H.-J. 3d Imaging of Water-Drop Condensation on Hydrophobic and Hydrophilic Lubricant-Impregnated Surfaces. *Sci. Rep.* **2016**, *6*, 23687.
(33) Jung, S.; Tiwari, M. K.; Poulikakos, D. Frost Halos from Supercooled Water Droplets. *Proc. Natl. Acad. Sci. U. S. A.* **2012**, *109*, 16073.

■ NOTE ADDED AFTER ASAP PUBLICATION

This paper was published ASAP on November 9, 2020, with an error in the Figure 1 scale bar. The corrected version was reposted on November 23, 2020.

https://dx.doi.org/10.1021/acs.nanolett.0c02956
Nano Lett. XXXX, XXX, XXX−XXX